Ocean Engineering 273 (2023) 113908

Contents lists available at ScienceDirect

Ocean Engineering

journal homepage: www.elsevier.com/locate/oceaneng

Numerical study on flow-induced vibration of two-degree-of-freedom staggered circular cylinders at subcritical Reynolds numbers

Tian Li [a,*], Takeshi Ishihara [b], Qingshan Yang [a], Qi Chen [a]

[a] School of Civil Engineering, Chongqing University, Chongqing, China
[b] Department of Civil Engineering, The University of Tokyo, Tokyo, Japan

ARTICLE INFO

Handling Editor: Prof. A.I. Incecik

Keywords:
Flow-induced vibration
Two-degree-of-freedom
Staggered circular cylinders
Numerical simulation
Added mass

ABSTRACT

In this study, the flow-induced vibration of two-degree-of-freedom staggered circular cylinders at subcritical Reynolds numbers is studied numerically with overset dynamic mesh. The streamwise spacing ratio S_x/D of 4 and the transverse spacing ratio S_y/D ranging from 0 to 2 are employed to explore the influence of staggered arrangement on the vibrations and fluid forces of cylinders. It is found the upstream cylinder mainly experiences the vortex-induced vibration while vortex-induced and wake-induced vibrations happen for the downstream one, which may be interfering or independent depending on the transverse spacing of cylinders. The phase lag between the displacement and fluid force of the downstream cylinder changes from 0° to 180° with the increasing of inflow velocity, which leads negative add mass and serves as the reason of wake-induced vibration. The theoretical formulae to estimate the critical velocity, fluid coefficient and vibration amplitude of wake-induced vibration are proposed and validated by the numerical simulations.

1. Introduction

The flow-induced vibration (FIV) of circular cylinders is common in ocean engineering and always leads fatigue damages. For the isolated circular cylinder, the vortex-induced vibration (VIV) occurs when the vortex-shedding frequency f_v approaches the structural natural frequency f_n (Sarpkaya, 2004; Martins and Avila, 2019; Ishihara and Li, 2020). For the cluster circular cylinders, there is a phenomenon that significant vibrations of the downstream cylinders are induced by the wake of upstream cylinders, which is regarded as wake-induced vibration (WIV). WIV is more harmful than VIV to the structures because it happens in a wider range of inflow velocity and its amplitude is generally larger (Li and Ishihara, 2021a).

To investigate the phenomenon of FIV of cluster circular cylinders, previous experimental studies started from the simplified setting of an elastically-mounted cylinder vibrating downstream a fixed same cylinder with tandem arrangement (Assi et al., 2010). It was found the WIV happens for small spacing ratio S_x/D and the VIV happens for large S_x/D. For the computational fluid dynamics (CFD) simulation of this issue, most researches were performed at Reynolds number lower than 500 where only VIV was observed (Carmo et al., 2011; Mysa et al., 2016). The WIV of tandem circular cylinders was successfully reproduced by a few studies at the subcritical Reynolds number (Nguyen et al., 2018; Li and Ishihara, 2021a).

Moreover, the circular cylinders in the staggered arrangement are more common than the tandem cylinders in the engineering applications. It is also more complicated because the interaction between the cylinders is always affected by spacing ratios between the cylinders in both streamwise and transverse directions. Through water tank or wind tunnel experiments for the freely-vibrating cylinder downstream a fixed staggered cylinder, it was found the downstream cylinder exhibited VIV and WIV depending on the streamwise and transverse spacings (Yagi et al., 2015; Du et al., 2018; Fukushima et al., 2021; Dao et al., 2022). Its mechanism was not fully explained since the experiments hardly measure the unsteady fluid forces of vibrating cylinders, while they can be easily obtained by the credible numerical simulations. However, few researches have been done for the FIV of staggered circular cylinders with numerical methods.

When both the upstream and downstream cylinders in the staggered arrangement are able to vibrate, the FIV becomes more complicated. Compared to the researches on the FIV of an elastically-mounted cylinder downstream a fixed upstream cylinder, there were fewer studies on the FIV of two freely-vibrating cylinders at subcritical Reynolds numbers. Some experimental and numerical investigation were done for

* Corresponding author.
E-mail address: li.tian@cqu.edu.cn (T. Li).

https://doi.org/10.1016/j.oceaneng.2023.113908
Received 24 November 2022; Received in revised form 3 February 2023; Accepted 6 February 2023
Available online 28 February 2023

the single-degree-of-freedom (SDOF) circular cylinders (Qin et al., 2019) and two-degree-of-freedom (2DOF) circular cylinders (Xu et al., 2021) in tandem arrangement at subcritical Reynolds numbers. Mittal and Kumar (2001) performed numerical simulation for the FIV of staggered 2DOF circular cylinders at Reynolds number of 100 and Griffith et al. (2017) did numerical study for the FIV of staggered SDOF circular cylinders at Reynolds number of 200. However, the FIV of 2DOF staggered circular cylinders at subcritical Reynolds numbers has not been studied comprehensively and its mechanism is still hard to understand.

In this study, the FIV of two identical 2DOF circular cylinders in staggered arrangement is studied. The unsteady shear stress transfer (SST) k-ω turbulence model is adopted to calculate the fluid force on vibrating cylinders at subcritical Reynolds numbers. In Section 2, the numerical methods of this research are introduced. Then, the FIV of staggered circular cylinders are investigated through the aspects of dynamic response, fluid force and theoretical analysis in Section 3. Finally, the conclusions are summarized in Section 4.

2. Numerical methods

In this section, the main information of the numerical method is given, including the governing equations of fluid and structure simulations, computational domain and numerical mesh.

2.1. Governing equations of fluid simulations

The flow around vibrating circular cylinders is simulated by the two-dimensional unsteady Reynolds-Averaged Navier-Stokes (RANS) model with dynamic mesh, where the continuity and momentum equations are :

$$\frac{\partial \rho \widetilde{u}_i}{\partial x_i} = 0 \tag{1}$$

$$\rho \frac{\partial \widetilde{u}_i}{\partial t} + \rho \frac{\partial \widetilde{u}_i}{\partial x_j}\left(\widetilde{u}_j - \widehat{u}_j\right) = -\frac{\partial \widetilde{p}}{\partial x_i} + \mu \frac{\partial}{\partial x_j}\left(\frac{\partial \widetilde{u}_i}{\partial x_j} + \frac{\partial \widetilde{u}_j}{\partial x_i}\right) - \frac{\partial \tau_{ij}}{\partial x_j} \tag{2}$$

where x, p and t stand for the coordinate, pressure and time respectively. u and $\widehat{u}$ indicate the velocities of fluid and moving mesh respectively. The subscripts i and j represent streamwise and vertical directions respectively, and the superscript "~" stands for the time averaged value. τ_{ij} is the time-averaged Reynolds stress modelled by

$$\tau_{ij} = -2\mu_t \widetilde{S}_{ij} + \frac{2}{3}\rho k \delta_{ij} \tag{3}$$

where δ_{ij} stands for the Kronecker symbol and $\widetilde{S}_{ij}$ is the mean rate-of-strain tensor defined as

$$\widetilde{S}_{ij} = \frac{1}{2}\left(\frac{\partial \widetilde{u}_i}{\partial x_j} + \frac{\partial \widetilde{u}_j}{\partial x_i}\right) \tag{4}$$

k represents the turbulence kinetic energy, and μ_t indicates the eddy viscosity calculated through the SST k-ω turbulence model (Menter, 1994) as

$$\mu_t = \rho \frac{k}{\omega} \tag{5}$$

where ω is the turbulence frequency.

Numerical simulations of this fluid-structure interaction problem are realized using the ANSYS Fluent 19.3 (ANSYS Inc, 2020) on the high-performance computing (HPC) system (AMD EPYC 7742 CPU, 128 cores, 256 GB memory). About 100 cases with different conditions are simulated where each case is simulated with 8 cores and costs about 120 hours of wall-clock-time.

Table 1
Structural parameters.

m^*	ζ	$m^*\zeta$	f_n	D
2.6	0.0036	0.009	0.4 Hz	0.05 m

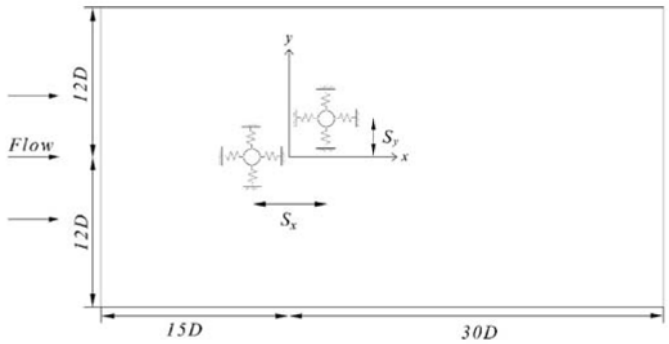

Fig. 1. Schematic of computational domain.

2.2. Modelling of structural system

The dynamic equations of the simulated 2DOF circular cylinders are defined as

$$m\ddot{x} + c\dot{x} + kx = F_D(t) \tag{6}$$

$$m\ddot{y} + c\dot{y} + ky = F_L(t) \tag{7}$$

where F_D and F_L stand for the transient drag and lift forces acting on the circular cylinders. m, c and k are the mass, damping and stiffness of cylinder respectively. The upstream and downstream circular cylinders are identical and their parameters in the numerical simulation refer to the experiments of Jauvtis and Williamson (2004) shown in Table 1, where $m^* = \frac{4m}{\rho\pi D^2 L}$ represents the mass ratio, $\zeta = \frac{c}{2\sqrt{k(m+m_A)}}$ and $f_n = \frac{1}{2\pi}\sqrt{\frac{k}{m+m_A}}$ stand for the damping ratio and structural natural frequency in the still water with $m_A = \frac{1}{4}\rho\pi D^2 L$ being the added mass in the still water. D represents the diameter of circular cylinders.

2.3. Numerical domain and mesh

The numerical domain is two-dimensional with width and depth being 45D and 24D respectively shown in Fig. 1. The cylinders are situated 15D downstream the inlet. The streamwise spacing S_x between two cylinders is set as 4D and the transverse spacing S_y is in the range of 0-2D.

The numerical mesh around the cylinders is presented in Fig. 2. $y+<1$ is kept to simulate the separation flow accurately. The boundary conditions at the inlet, outlet, transverse sides and cylinder surface are defined as uniform velocity, zero diffusive outflow, symmetric and no-slip wall respectively. 2D k-ω model with sliding dynamic mesh was used in Li and Ishihara (2021b), but failed to reproduce the VIV of 2DOF circular cylinder. In this study, the 2D k-ω model with overset dynamic mesh is adopted to simulate the VIV and WIV of 2DOF circular cylinders at subcritical Reynolds numbers. This method can accurately reproduce large-amplitude vibrations and relative motions of multiple bodies, and its efficiency is much higher than the 3D LES (Ishihara and Li, 2020; Li and Ishihara, 2021a). Each circular cylinder is surrounded by the O-type mesh which overlaps with the background mesh. Most parts of the overlapped meshes are deleted after oversetting and only the fringe meshes are kept for the variable interpolation.

The numerical convergence test is performed by the simulated vibration amplitude of downstream circular cylinder with $S_x = 4$ and $S_y =$

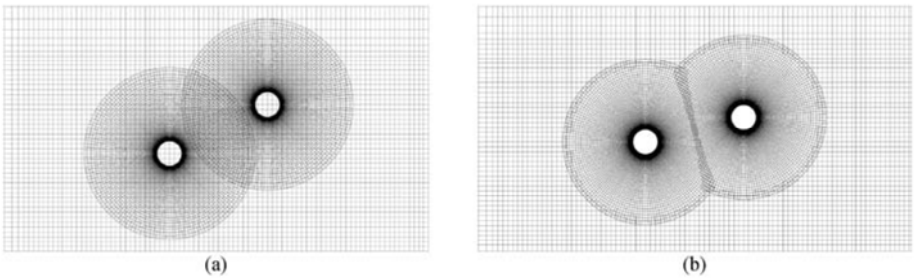

Fig. 2. Numerical mesh around the cylinders for (a) before overset and (b) after overset.

Table 2
Mesh convergence test.

	Mesh quantity	A_x/D	A_y/D
Mesh1	31380	0.58422	0.67768
Mesh2	41984	0.60188 (3.0%)	0.70931 (4.7%)
Mesh3	86400	0.60947 (1.3%)	0.68657 (3.2%)

Table 3
Time step dependency test.

Time step	A_x/D	A_y/D
0.002s	0.61070	0.77676
0.001s	0.60188 (1.4%)	0.70931 (8.7%)
0.0005s	0.58847 (2.2%)	0.71877 (1.3%)

1.5 at $U_r = 20$, corresponding to the large amplitude of WIV, where $U_r = \frac{U}{f_n D}$ represents the reduced velocity. The streamwise and transverse vibration amplitudes of cylinder A_x and A_y are estimated by $\sqrt{2}$ times of the standard deviation of displacement and non-dimensionalized by the cylinder diameter D. Over 50 vibration periods are simulated to get reasonable statistics. Three numerical meshes with various quantities and three time steps are tested as shown in Tables 2 and 3, and the change ratios of simulated vibration amplitude are presented in brackets. It shows the differences among simulated values decrease with the increasing mesh quantities within 5%, which satisfies the engineering criterion of convergence. Mesh2 is selected in the present research considering both accuracy and efficiency. The differences among simulated vibration amplitudes generally decrease with the decreasing time step and the difference between simulated vibration amplitudes with time step of 0.001s and 0.0005s is smaller than 3%, thus the time step of 0.001s is used in the later research considering both accuracy and efficiency.

3. Results and discussion

The characteristics and mechanism of FIV of 2DOF staggered circular cylinders at subcritical Reynolds number are systematically investigated in this section. The numerical methods are first validated, then the vibration amplitude and trajectory are analyzed, after that the fluid forces and flow fields are discussed, and finally the wake-induce vibration is analyzed theoretically.

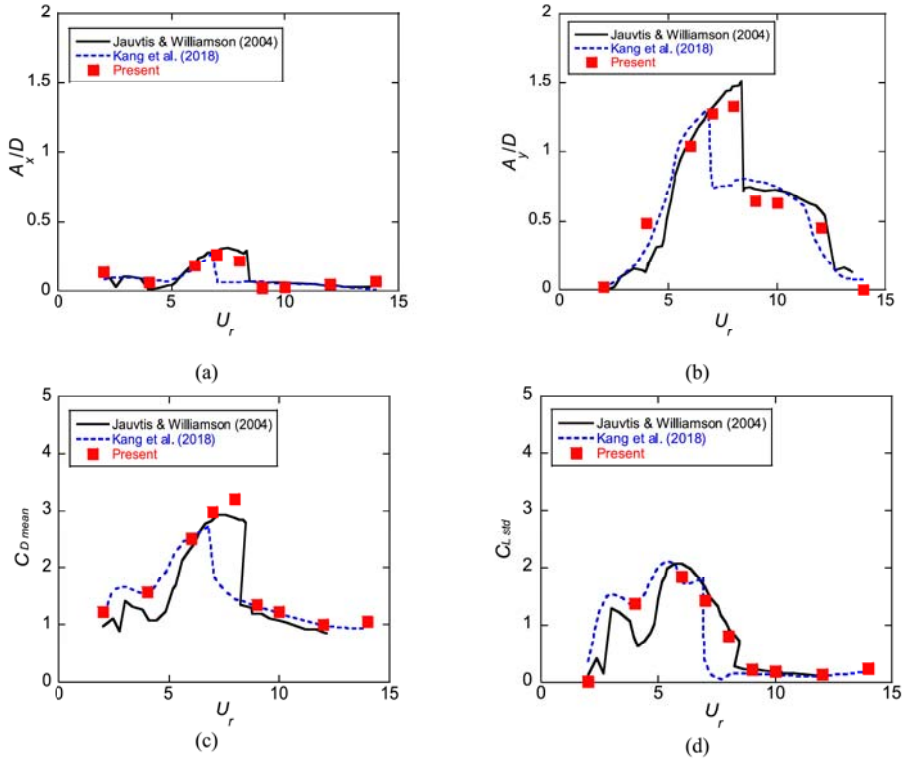

Fig. 3. Variations of (a) streamwise amplitude A_x/D, (b) transverse amplitude A_y/D, (c) mean drag coefficient $C_{D\,mean}$ and (d) fluctuating lift coefficient $C_{L\,std}$ with U_r for 2DOF isolated circular cylinder.

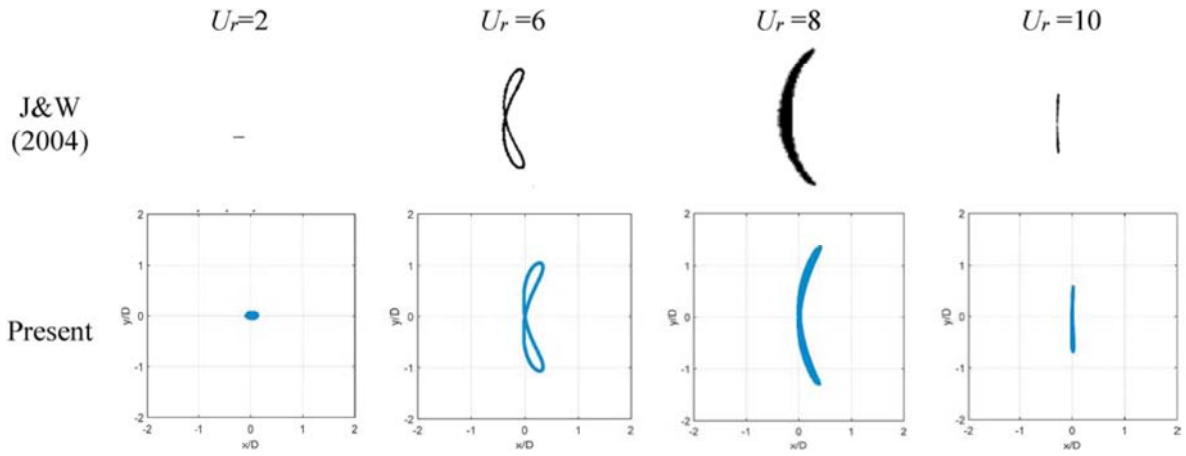

Fig. 4. FIV trajectories of 2DOF isolated circular cylinder.

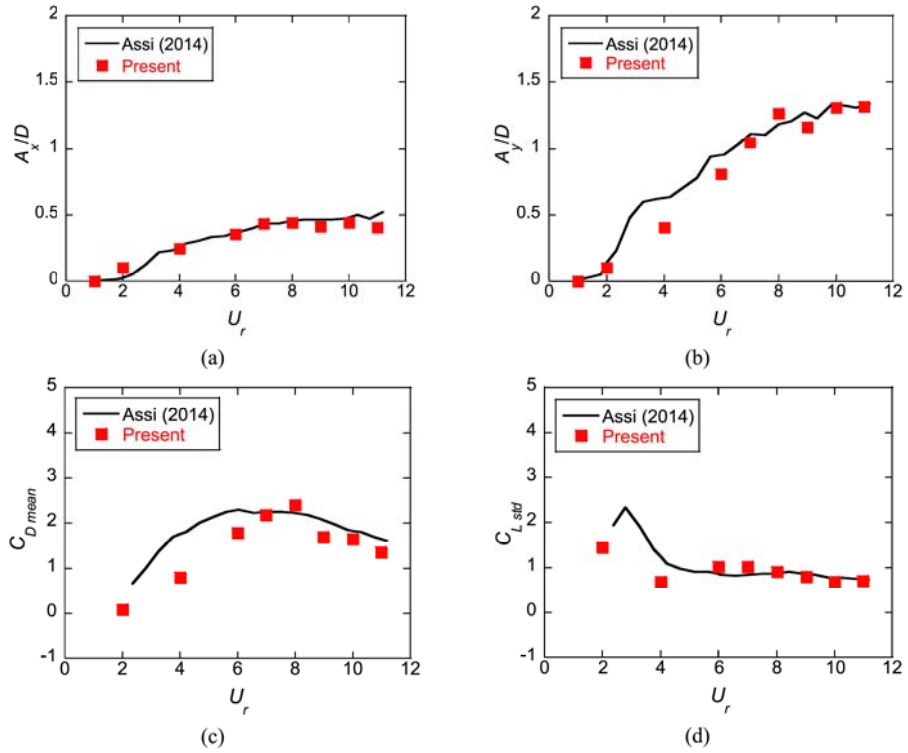

Fig. 5. Variations of (a) streamwise amplitude A_x/D, (b) transverse amplitude A_y/D, (c) mean drag coefficient $C_{D\ mean}$ and (d) fluctuating lift coefficient $C_{L\ std}$ with U_r for the downstream circular cylinder of two 2DOF tandem circular cylinders with $S_x = 4D$ and structural parameters of Assi (2014).

3.1. Validation for the numerical methods

The present numerical methods are firstly validated for simulating the FIV of a 2DOF isolated circular cylinder. The vibration amplitudes and fluid force ceofficients of the isolated circular cylinder are compared to the experimental data by Jauvtis and Williamson (2004) and the numerical data by Kang et al. (2018). The numerical settings are same as the experimental ones, where the reduced velocity U_r ranges from 2 to 14 and the Reynolds number R_e ranges from 2000 to 14000. The simulated non-dimensional streamwise and transverse vibration amplitudes A_x/D and A_y/D as well as the mean drag coefficient $C_{D\ mean}$ and fluctuating lift coefficient $C_{L\ std}$ are shown in Fig. 3, and the vibration trajectories are provided in Fig. 4, indicating that the vibration amplitude, fluid force coefficient and vibration trajectories are well predicted by the present numerical method, while those predicted by Kang et al. (2018) underestimated the vibration amplitude around $U_r = 8$.

In addition, the present numerical method is also validated for reproducing the FIV of two 2DOF tandem circular cylinders with $S_x = 4D$. The characteriscs of vibration and fluid forces of the downstream circular cylinder are compared to the experimental data of Assi (2014) in Fig. 5 and the numerical data of Xu et al. (2021) in Fig. 6, where the numerical setting is same as the references with $R_e = 3000–24000$ and 2000–14000 respectively. It is found that the simulated vibration amplitudes and fluid force coefficients show favorable agreement with those from previous research. To the knowledge of authors, this is the first numerical study for the WIV of 2DOF circular cylinders at subcritical Reynolds numbers with the validation by experimental data of WIV.

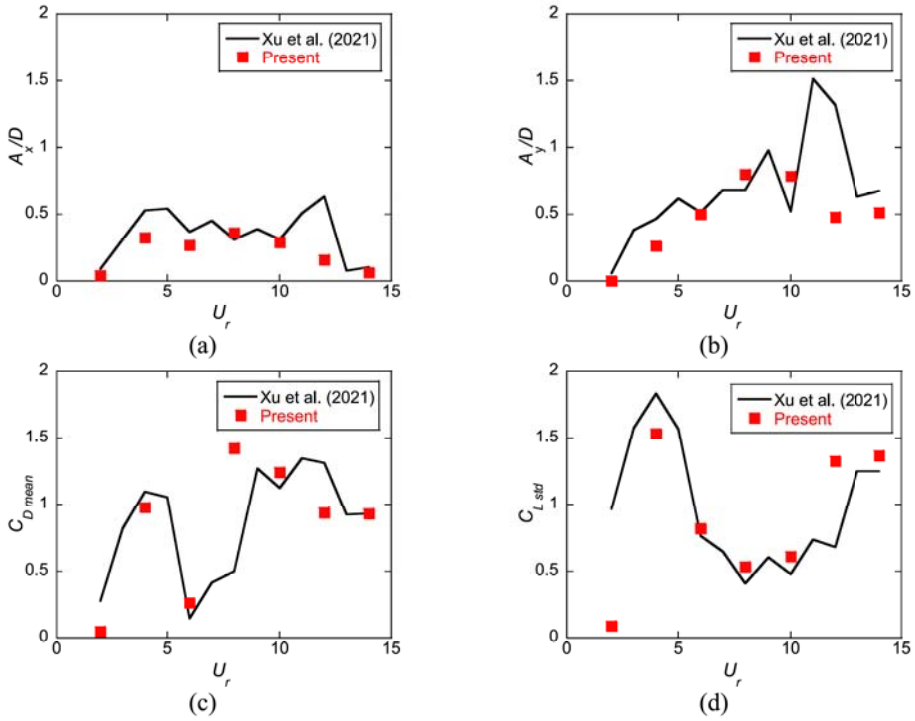

Fig. 6. Variations of (a) streamwise amplitude A_x/D, (b) transverse amplitude A_y/D, (c) mean drag coefficient $C_{D\,mean}$ and (d) fluctuating lift coefficient $C_{L\,std}$ with U_r for the downstream circular cylinder of two 2DOF tandem circular cylinders with $S_x = 4D$ and structural parameters of Xu et al. (2021).

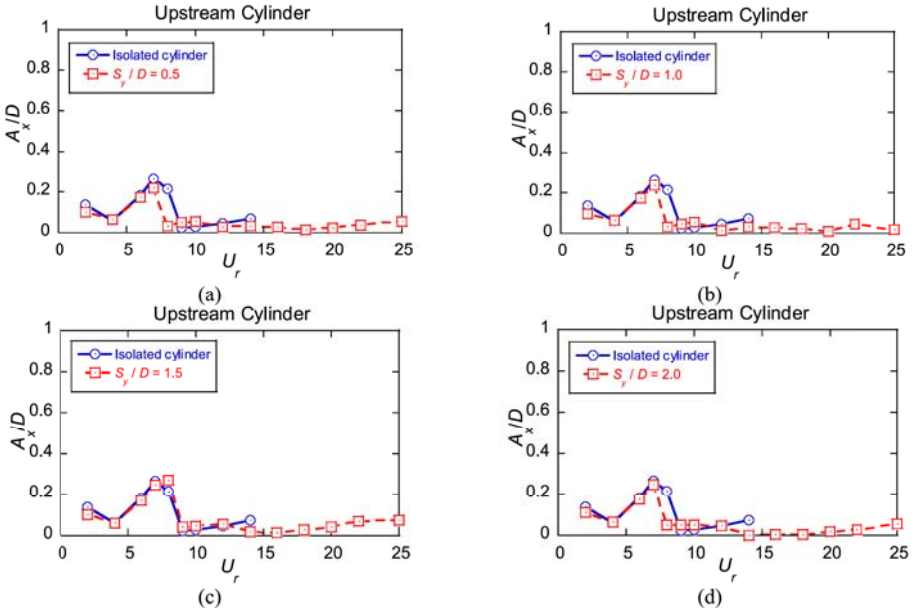

Fig. 7. Variations of streamwise vibration amplitude A_x/D of upstream circular cylinder with U_r for (a) $S_y/D = 0.5$, (b) $S_y/D = 1.0$, (c) $S_y/D = 1.5$ and (d) $S_y/D = 2.0$.

3.2. Vibration amplitude and trajectory

The vibration amplitude and trajectory of two 2DOF staggered circular cylinders with various transverse spacing ratios are then analyzed. The Reynolds number R_e ranges from 2000 to 25000 and belongs to the subcritical regime, which is the common range of the engineering practice. The variations of streamwise vibration amplitude A_x/D with U_r are displayed in Figs. 7 and 8 with the vibration amplitude of an identical isolated cylinder for comparison. It is seen that the streamwise vibration amplitudes of the upstream cylinder at $S_y/D = 0.5$, 1.0, 1.5 and 2.0 are similar to those of the isolated cylinder that the vibration amplitude generally increases with the reduced velocity for $U_r < 7$, and then decreases and keeps stable, shows the apparent VIV phenomenon. Compared to the isolated cylinder, the amplitude of upstream cylinder decreases faster for $U_r > 7$. On the other hand, there are multiple peaks in the U_r-A_x/D curve of the downstream cylinder, which is distinguished from that of the isolated or upstream cylinder and was also found in previous researches (Yu et al., 2016; Armin et al., 2018). The streamwise vibration amplitude of the downstream cylinder is slightly higher than that of the isolated cylinder for $4 \leq U_r \leq 6$, which belongs to the VIV branch. As U_r increases, A_x/D of the downstream cylinder first decreases and then increases again and shows a divergence trend, which shows the

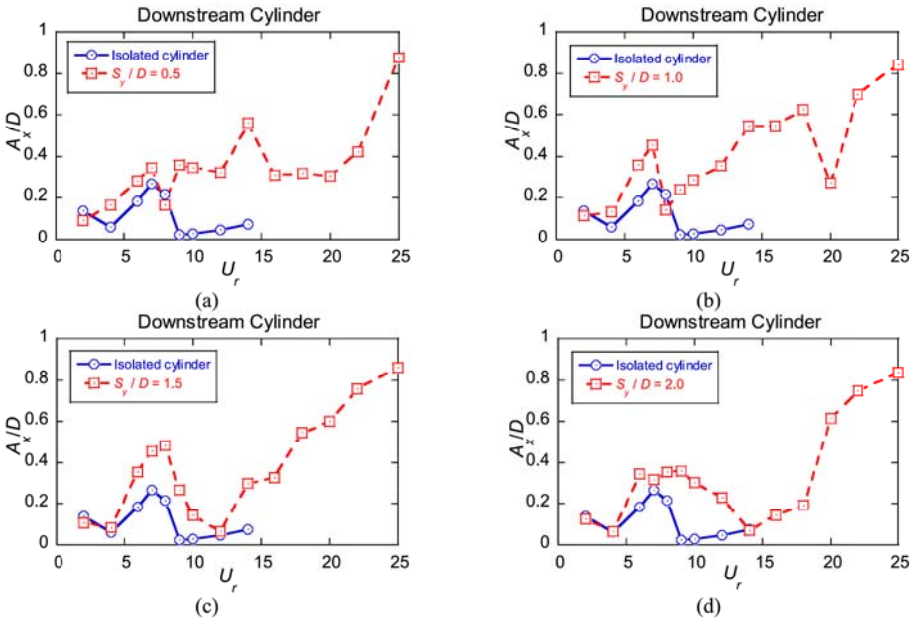

Fig. 8. Variations of streamwise vibration amplitude A_x/D of downstream circular cylinder with U_r for (a) $S_y/D = 0.5$, (b) $S_y/D = 1.0$, (c) $S_y/D = 1.5$ and (d) $S_y/D = 2.0$.

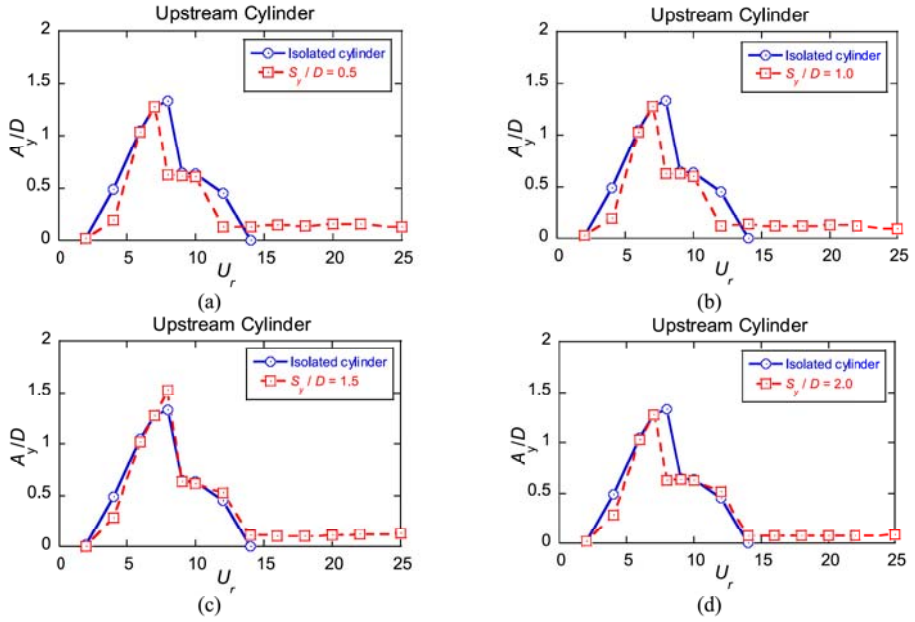

Fig. 9. Variations of transverse vibration amplitude A_y/D of upstream circular cylinder with U_r for (a) $S_y/D = 0.5$, (b) $S_y/D = 1.0$, (c) $S_y/D = 1.5$ and (d) $S_y/D = 2.0$.

features of the WIV branch. As the S_y/D increases, the critical reduced velocity of the WIV branch generally increases, results that the VIV and WIV branches are interfered for the $S_y/D \leq 1$ and independent for the $S_y/D > 1$.

The variations of transverse amplitude A_y/D with U_r are displayed in Figs. 9 and 10 also with the vibration amplitude of an identical isolated cylinder for comparison. It is seen that the transverse vibration amplitudes of the upstream cylinder are also similar to those of the isolated cylinder and show the VIV phenomenon. Compared to the isolated cylinder, the peak of vibration amplitude decreases earlier for $U_r > 7$. On the other hand, the transverse vibration amplitudes of the downstream cylinder are lower than those of the isolated cylinder in the VIV branch of $4 \leq U_r \leq 6$. As U_r increases, A_y/D of the downstream cylinder first decreases, then increases again and shows a divergence trend, which belongs to the WIV branch. As the S_y/D increases, the critical reduced velocity of the WIV branch also increases, results that the VIV and WIV branches are interfered for the $S_y/D \leq 1$ and independent for the $S_y/D > 1$.

The variations of the vibration trajectory with the reduced velocity U_r at various S_y/D for the two cylinders are shown in Fig. 11. It is seen that the vibration trajectory of the upstream cylinder is similar to that of the isolated 2DOF cylinder (Li and Ishihara, 2021b). For $U_r = 2$, the upstream cylinder is subject to the streamwise vibration. For $2 < U_r \leq 6$, the vibration trajectory develops into figure-eight shape indicating the streamwise vibration frequency is twice of the transverse one. When A_x/D and A_y/D reach their maxima in $6 < U_r \leq 8$, the trajectory of the upstream cylinder becomes the crescent shape. When U_r continues to increase in $8 < U_r \leq 12$, the upstream cylinder becomes the transverse

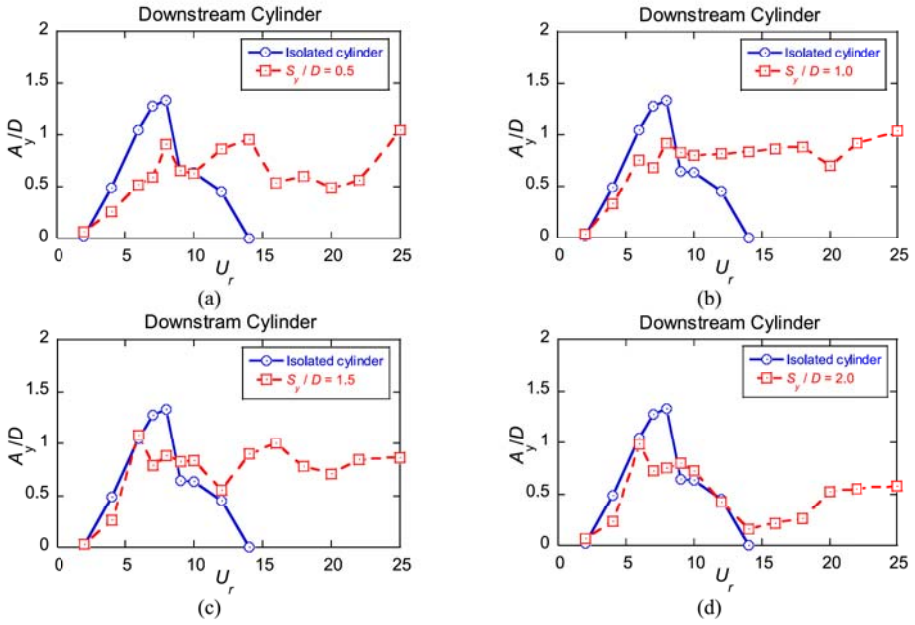

Fig. 10. Variations of transverse vibration amplitude A_y/D of downstream circular cylinder with U_r for (a) $S_y/D = 0.5$, (b) $S_y/D = 1.0$, (c) $S_y/D = 1.5$ and (d) $S_y/D = 2.0$.

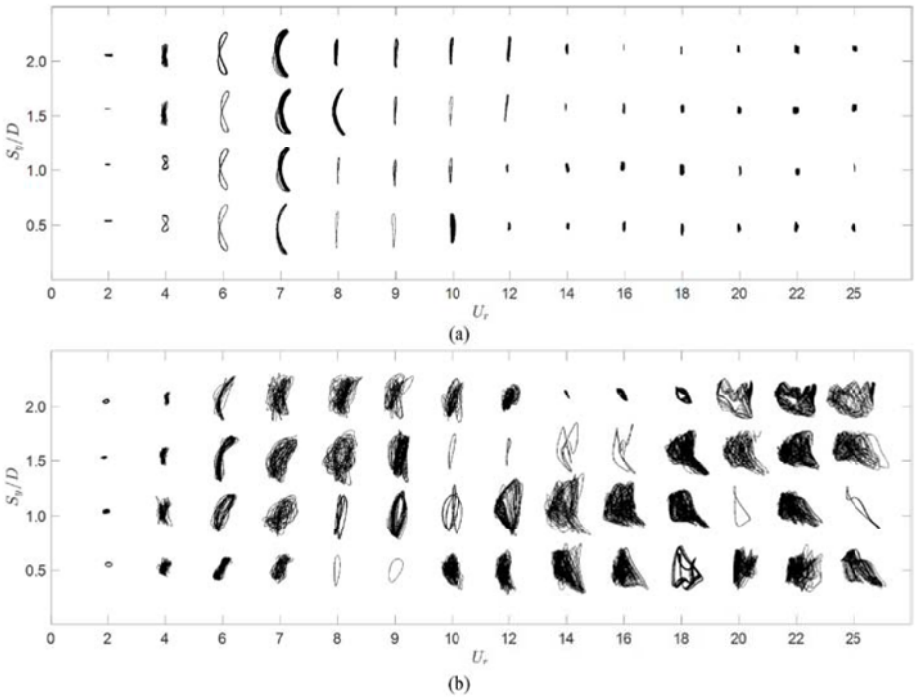

Fig. 11. Variations of the vibration trajectories with U_r at various S_y/D for (a) upstream circular cylinder and (b) downstream circular cylinder.

vibration. When $U_r > 12$, the vibrations in both directions are not obvious. Compared to the upstream cylinder, the vibration trajectory of the downstream cylinder is more unstable and irregular. At most range of U_r, the downstream cylinder vibrates in nonperiodic trajectories composed of figure-eight, oval and elliptical trajectories. Only for the range between the gap of VIV and WIV branches, the vibration of the downstream cylinder becomes relatively periodic.

3.3. Fluid forces and flow fields

The variations of mean drag coefficient $C_{D\ mean}$ and fluctuating lift coefficient $C_{L\ std}$ of the freely-vibrating staggered cylinder with U_r are displayed in Fig. 12 with the force coefficients of the freely-vibrating isolated cylinder for comparison. It is found that the $C_{D\ mean}$ and $C_{L\ std}$ of the upstream cylinder are similar to those of the isolated cylinder. The peak of $C_{D\ mean}$ on the upstream cylinder are smaller and decreases earlier for $U_r > 7$ compared to the isolated cylinder. On the other hand, $C_{D\ mean}$ and $C_{L\ std}$ on the downstream cylinder are different from those of the isolated cylinder. Compared with the isolated cylinder, the $C_{D\ mean}$ and $C_{L\ std}$ of the downstream cylinder at the VIV branch are generally lower, while the $C_{L\ std}$ of the downstream cylinder at the WIV branch are generally higher. The difference is more significant for the smaller S_y/D

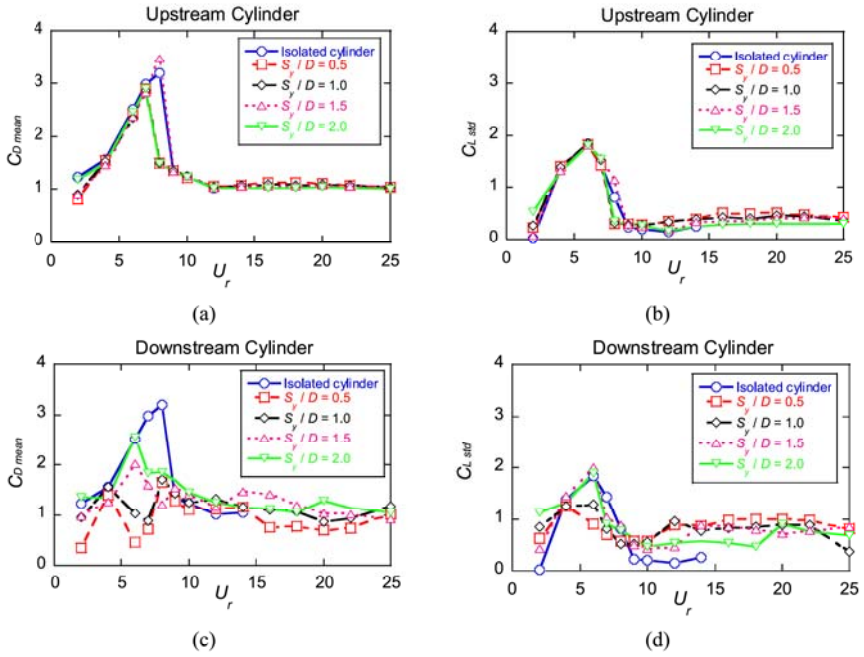

Fig. 12. Variations of (a) mean drag coefficient $C_{D\ mean}$ of upstream circular cylinder, (b) fluctuating lift coefficient $C_{L\ std}$ of upstream circular cylinder, (c) mean drag coefficient $C_{D\ mean}$ of downstream circular cylinder, and (d) fluctuating lift coefficient $C_{L\ std}$ of downstream circular cylinder with U_r.

Table 4
Comparison of fluid force coefficient of stationary staggered cylinders simulated by 2D k-ω and 3D LES model.

Model	S_y/D	Upstream cylinder		Downstream cylinder	
		$C_{D\ mean}$	$C_{L\ std}$	$C_{D\ mean}$	$C_{L\ std}$
2D k-ω	0.5	1.4821	1.2027	0.3646	0.9808
	1.0	1.4789	1.1942	0.6353	0.8521
3D LES	0.5	1.2077	0.5182	0.6154	0.8036
	1.0	1.2533	0.7884	0.5697	0.8281

because of the larger wake effect.

In addition, the fluid force coefficients on the stationary staggered circular cylinders are also simulated by the 2D k-ω model and compared with the results by the 3D LES model in the previous research (Li and Ishihara, 2021a) as shown in Table 4. It is found that the 2D k-ω model generally overestimates the fluid force coefficients of the stationary staggered circular cylinders, because the three-dimensionality of flow field around stationary circular cylinders cannot be simulated with 2D model (Li and Ishihara, 2021b). Only the $C_{D\ mean}$ of downstream cylinder at $S_y/D = 0.5$ is underestimated by the 2D k-ω model because the strength of vortices shed from the upstream cylinder and the suction on the front surface of the downstream cylinder are overestimated. Even though, the 2D k-ω model is effective to reproduce the vibration amplitude of FIV as shown in Figs. 3–6 because the two-dimensionality of flow field around vibrating circular cylinders increases.

The contours of logarithmic normalized power spectral density (PSD) of the drag and lift coefficients of the two cylinders are presented in Fig. 13 to identify the dominant vortex shedding frequencies f_{C_D} and f_{C_L}. The results of $S_y/D = 1.5$ are shown for instance. It is found for both drag and lift coefficients of the two cylinders, the lock-in phenomenon happens in the VIV branch. The frequency of drag force f_{C_D} is locked in about twice the structural natural frequency and the frequency of lift force f_{C_L} is locked in about the structural natural frequency. The increase of f_{C_D} and f_{C_L} in the lock-in regime is due to the negative added mass which will be discussed in Section 3.4. In the WIV branch, the frequency of drag force on the upstream cylinder follows $S_t = 0.38$ and the frequency of lift force on the upstream cylinder follows $S_t = 0.19$, while both the frequencies of drag and lift forces on the downstream cylinder follows the $S_t = 0.19$. Multiple frequencies are observed in both drag and lift coefficient of the two cylinders in the VIV branch, equal one, two, three and four times of the structural natural frequency, while only one frequency generally dominates in the WIV branch.

The time histories of transverse displacement y/D and lift coefficient C_L as well as contours of vorticity ω_z at four phases in a vibration period for the staggered circular cylinders with $S_y/D = 1.5$ are presented in Fig. 14, where ω_z is calculated by $(\partial u_y/\partial x\text{-}\partial u_x/\partial y)/(U/D)$, T stands for the vibration period and t_0 indicates the time when the downstream cylinder passes the balance position with positive velocities. The results of $U_r = 2$, 6, 8, 14, 18, and 22 are provided for example. It is found that at $U_r = 2$, two parallel vortices shed from the upstream cylinder per vibration period and form the side-by-side 2S vortex shedding mode. These vortices will pass nearby the downstream cylinder and increase the scale of vortices shed from the downstream cylinder, resulting in larger lift coefficients of the downstream cylinder. At $U_r = 6$, two single opposite-sign vortices shed from the upstream and downstream cylinders per vibration period, which forms the 2S pattern. Under the interference of vortices shed from the upstream cylinder, the vortices shed from the downstream cylinder also have larger scales and result in larger lift coefficients. At $U_r = 8$, the second vortex shedding happens for the upstream cylinder, which forms the 2T pattern and high-frequency fluctuation of lift coefficients, following the description in Li and Ishihara (2021b). The vortices shed from the upstream cylinder will merge with those shed from the downstream cylinder and forms large-scale vortices in the wake of downstream cylinder. As a result, the lift coefficient of the downstream cylinder fluctuates with large amplitudes but low frequency. At $U_r = 14$–25, two pairs of opposite-sign vortices generally shed per vibration period from the upstream and downstream cylinders. They form the 2P pattern and lead the out-of-phase between displacement and lift coefficient, which is the main feature of WIV.

3.4. Theoretical analysis of wake-induced vibration

The dynamic equation of the circular cylinder with fluid forces decomposition in the transverse direction is expressed as (Li et al., 2018; Ishihara and Li, 2020)

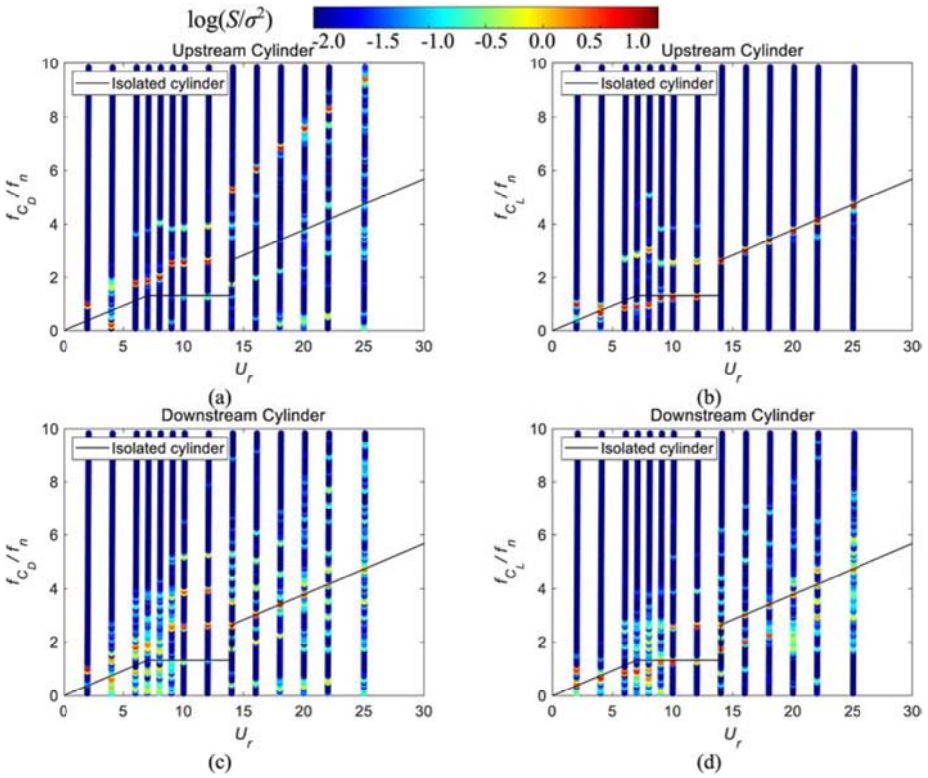

Fig. 13. Normalized power spectral densities of (a) drag coefficient of upstream circular cylinder, (b) lift coefficient of upstream circular cylinder, (c) drag coefficient of downstream circular cylinder, and (d) lift coefficient of downstream circular cylinder for $S_y/D = 1.5$.

$$m\ddot{y} + c\dot{y} + ky = F_L(t) = F_b(t) + F_u(t, y, \dot{y}, \ddot{y}) \tag{8}$$

where F_b represents the buffeting force and F_u stands for the unsteady fluid force as a function of time t, displacement y, velocity $\dot{y}$ and acceleration $\ddot{y}$.

F_u can be decomposed into the in-phase force F_m and the out-of-phase force F_c based on the orthogonality of y (or $\ddot{y}$) and $\dot{y}$ as

$$F_u(t, y, \dot{y}, \ddot{y}) = F_m(t, y, \ddot{y}) + F_c(t, \dot{y}) \tag{9}$$

F_m and F_c are linearly approximated as

$$F_m(t, y, \ddot{y}) = -m_a\ddot{y} \tag{10}$$

$$F_c(t, \dot{y}) = -c_a\dot{y} \tag{11}$$

where m_a and c_a are added mass and damping respectively because they cause changes in the total mass and damping of system. Then the dynamic equation of the circular cylinder is rewritten as

$$(m + m_a)\ddot{y} + (c + c_a)\dot{y} + ky = F_b(t) \tag{12}$$

m_a and c_a can be identified through the orthogonality of $\ddot{y}$ and $\dot{y}$ as

$$m_a = -\frac{\int_0^T F_L(t)\ddot{y}(t)dt}{\int_0^T \ddot{y}(t)^2 dt} \tag{13}$$

$$c_a = -\frac{\int_0^T F_L(t)\dot{y}(t)dt}{\int_0^T \dot{y}(t)^2 dt} \tag{14}$$

The displacement y and lift force F_L of the vibrating circular cylinder under vibration can be approximated by harmonic formulae as

$$y = A\ sin(\omega t) \tag{15}$$

$$F_L = \frac{1}{2}\rho U^2 DL\widehat{C}_L\ sin(\omega t + \varphi) \tag{16}$$

where $\widehat{C}_L$ is the amplitude of lift coefficient C_L and φ is the phase delay between the F_L and y.

Based on the quasi-steady theory, F_L depends on the relative position of the downstream cylinder, thus $\widehat{C}_L$ equals to the mean lift coefficient $C_{L\ mean}$ of the fixed downstream cylinder at the transverse position equaling the vibration amplitude A. It is found $C_{L\ mean}$ is linear to S_y for $-0.5 < S_y < 0.5D$ and $S_x = 4D$ (Li and Ishihara, 2021a), so $\widehat{C}_L$ is modelled as

$$\widehat{C}_L = \alpha\frac{A}{D} \tag{17}$$

where α is the absolute slope of $C_{L\ mean}$ to S_y/D. The relationship between $\widehat{C}_L$ and A becomes nonlinear for large A, which will be further considered in our future work.

Combining Eqs. (13)-(17), the added mass and damping are derived as

$$m_a = \frac{1}{2\omega^2}\rho U^2 L\alpha\cos(\varphi) \tag{18}$$

$$c_a = -\frac{1}{2\omega}\rho U^2 L\alpha\sin(\varphi) \tag{19}$$

It means the magnitudes of m_a and c_a increase with the inflow velocity U, the absolute slope of lift coefficient α and cosine/sine of phase lag φ.

As illustrated in Fig. 15, the phase lag φ jumps from 0° to 180° in the

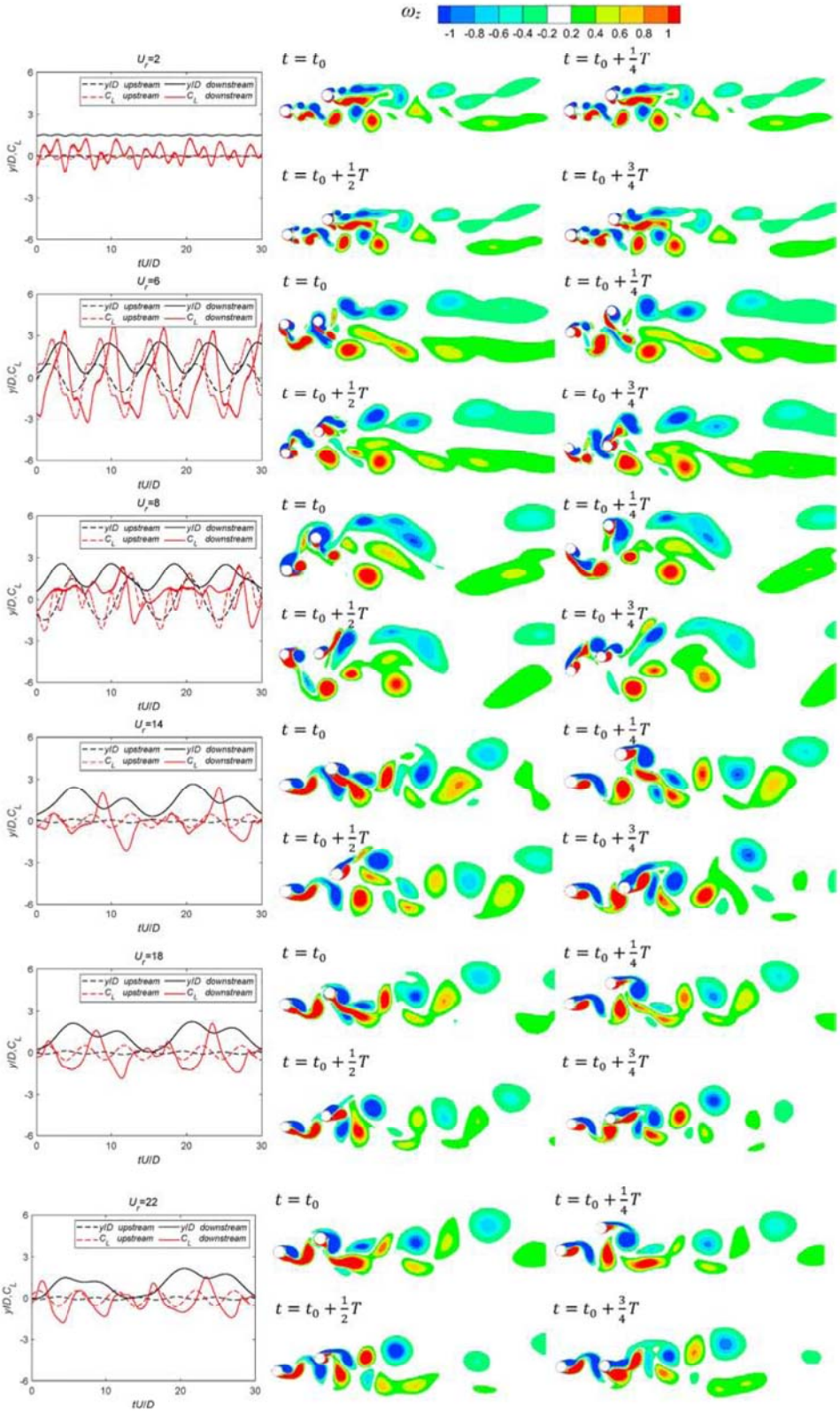

Fig. 14. Time histories of transverse displacement y/D and lift coefficient C_L and contours of vorticity ω_z for the circular cylinders with $S_y/D = 1.5$.

VIV branch, results m_a changes from positive to negative after the VIV branch and c_a is close to null except in the VIV branch. After the VIV branch, the magnitude of negative added mass increases and the total system mass $m_a + m$ decreases as the inflow velocity U increases. When U researches a critical value, $m_a = -m$ and the total system mass becomes zero, then WIV branch is developed with significant vibration amplitude. The critical velocity of WIV u_{WIV} is defined at this condition as

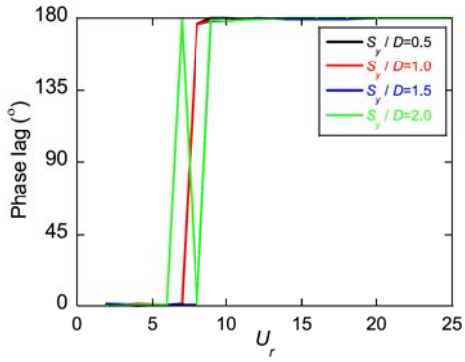

Fig. 15. Phase lags between lift force and displacement of the downstream cylinder.

$$m-\frac{1}{2\alpha^2}\rho u_{WIV}{}^2 L\alpha=0 \tag{20}$$

The non-dimensional critical velocity of WIV U_{WIV} is then derived as

$$U_{WIV}=\frac{u_{WIV}}{f_n D}=\sqrt{\frac{2\pi^3}{\alpha}m^*} \tag{21}$$

The numerically simulated variations of added mass ratio m_a^*, add damping ratio ζ_a and total vibration amplitude $A=\sqrt{A_x{}^2+A_y{}^2}$ with reduced velocity U_r for various S_y/D are shown in Fig. 16. As the lift slope α equals 0.58 for $S_x/D=4$ according to Li and Ishihara (2021a), the critical reduced velocity of WIV U_{WIV} predicted by the proposed theoretical model and the critical reduced velocity of VIV $U_{VIV}=1/S_t$ are also denoted. The added mass ratio m_a^* is defined as m_a normalized by the displaced fluid mass and the added damping ratio ζ_a is defined as c_a normalized by the critical damping as

$$m_a^*=-\frac{\int_0^T F_L(t)\ddot{y}(t)dt}{\int_0^T \ddot{y}(t)^2 dt}\Big/\left(\frac{1}{4}\rho\pi D^2 L\right) \tag{22}$$

$$\zeta_a=-\frac{\int_0^T F_L(t)\dot{y}(t)dt}{\int_0^T \dot{y}(t)^2 dt}\Big/\left(2\sqrt{k(m+m_A)}\right) \tag{23}$$

The numerical results prove the theoretical inference that the added mass ratio m_a^* is positive before the VIV branch and decreases to be negative in the WIV branch. It approaches the negative structural mass ratio of circular cylinder when the WIV is developed. In the VIV branch, the added damping ratio ζ_a is negative and close to the negative value of structural damping ratio, and the negative added mass ratio in the lock-

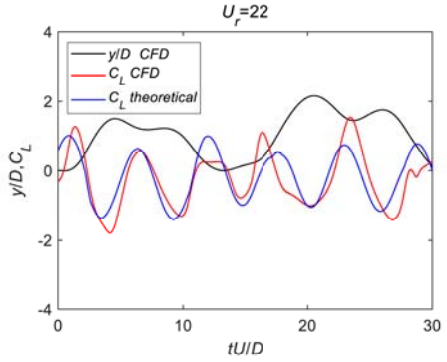

Fig. 17. Comparison of theoretically predicted and numerical simulated lift coefficients for $S_y/D=1.5$ and $U_r=22$.

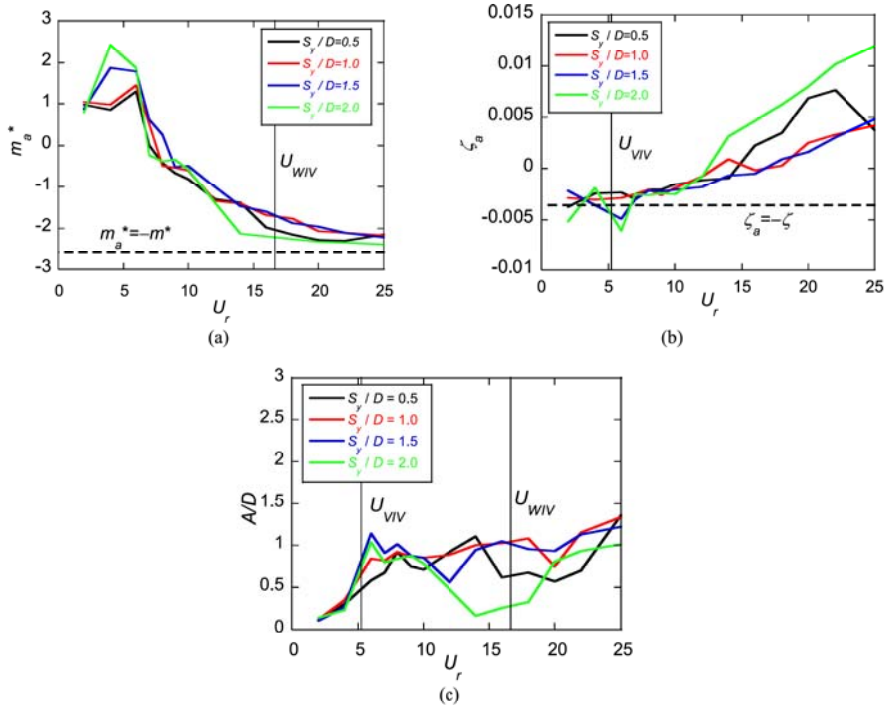

Fig. 16. Variations of (a) added mass ratio, (b) added damping ratio and (c) total vibration amplitude with U_r for circular cylinders.

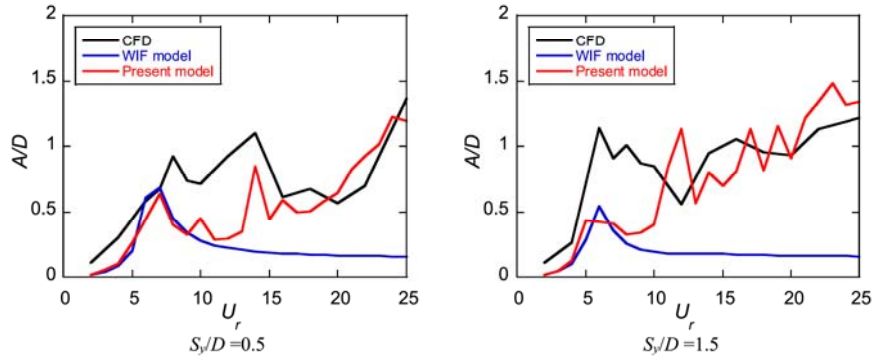

Fig. 18. Comparison of theoretically predicted and numerical simulated vibration amplitude for $S_y/D = 0.5$ and 1.5.

in regime results that the f_{C_D}/f_n and f_{C_L}/f_n there increase with U_r as shown in Fig. 13. It is obvious that the VIV is caused by the negative added damping, while the WIV is induced by the negative added mass.

Equations (6) and (7) are further solved using the fourth-order Runge-Kutta method, where both the streamwise and transverse vibrations as well as lift and drag forces are considered. The mean components of fluid force coefficients $C_{D\ mean}(x,y)$ and $C_{L\ mean}(x,y)$ are calculated based on the quasi-steady theory and the experimental data of fluid force coefficients for static staggered cylinders (Li et al., 2019), the fluctuating component of drag force is neglected due to its small magnitude, and the fluctuating component of lift force is modelled as harmonic in time at the angler frequency ω as

$$F_D(t) = \frac{1}{2}\rho U^2 DLC_{D\ mean}(x,y) \tag{24}$$

$$F_L(t) = \frac{1}{2}\rho U^2 DL\left[C_{L\ mean}(x,y) + C_{L\ std}(S_x,S_y)\cdot\sin(\omega t)\right], \omega = S_t\cdot U \Big/ D \tag{25}$$

The transient lift force coefficient predicted by this theoretical model are compared with those simulated by the present CFD model for $S_y/D = 1.5$ and $U_r = 22$ as shown in Fig. 17 for example. It is found that the fluid the force coefficient during WIV can be favorably estimated by this theoretical model.

The theoretically predicted vibration amplitudes are also compared with the numerical simulated ones and those estimated by the quasi-steady-theory-based wake-induced flutter model (Price and Piperni, 1988; Li et al., 2019). The results for $S_y/D = 0.5$ and 1.5 are shown in Fig. 18 for example. It is found that the present theoretical model qualitatively reproduces the trend of WIV and is better than the quasi-steady-theory-based wake-induced flutter model. The VIV branch cannot be reproduced because the unsteady effect there has not been included. The high-order unsteady fluid dynamic derivatives should be considered to improve the accuracy (Yagi et al., 2015; Oka and Ishihara, 2020; Fukushima et al., 2021; Fehér and Avila, 2022), which will be investigated in the next step.

4. Conclusions

The flow-induced vibration of two-degree-of-freedom staggered circular cylinders at subcritical Reynolds numbers is investigated by numerical simulations. The vibration amplitude, fluid forces, trajectories, flow fields and theoretical models are studied. The main conclusions are summarized as follows:

(1) The upstream cylinder mainly experiences the vortex-induced vibration (VIV) when the vortex shedding frequency approaches the structural natural frequency, while VIV and wake-induced vibration (WIV) occur in the downstream cylinder, which may be interfered or independent depending on the transverse spacing of the two cylinders.
(2) The mean drag and fluctuating lift coefficients of the downstream cylinder in the VIV branch are generally lower than those of the upstream cylinder, while the fluctuating lift coefficient of the downstream cylinder at the WIV are generally higher than those of the upstream cylinder, and the difference is larger for the smaller S_y/D. 2P vortex shedding pattern and the out-of-phase between displacement and lift coefficient are the main feature of WIV
(3) The phase lag between the displacement and fluid force of the downstream cylinder changes from 0° to 180° with the increasing inflow velocity, which leads negative add mass and serves as the reason of wake-induced vibration. The theoretical formulae to estimate the critical velocity, fluid coefficient and vibration amplitude of wake-induced vibration are proposed and validated by the numerical simulations.

CRediT authorship contribution statement

Tian Li: Conceptualization, Methodology, Investigation, Software, Data curation, Visualization, Validation, Writing – original draft, Writing – review & editing. **Takeshi Ishihara:** Conceptualization, Methodology, Supervision, Writing – review & editing. **Qingshan Yang:** Project administration, Writing – review & editing. **Qi Chen:** Investigation, Software, Data curation, Visualization.

Declaration of competing interest

The authors declare that they have no known competing financial interests or personal relationships that could have appeared to influence the work reported in this paper.

Data availability

Data will be made available on request.

Acknowledgement

Supports from National Natural Science Foundations of China (52221002, 52208463), 111 Project of China (B18062), Postdoctoral Research Foundation of China (2021M693737) and Chongqing Science and Technology Bureau (cstc2021yszx-jcyj0009) are gratefully acknowledged.

References

Armin, M., Khorasanchi, M., Day, S., 2018. Wake interference of two identical oscillating cylinders in tandem: an experimental study. Ocean Eng. 166, 311–323.
ANSYS Inc, 2020. ANSYS FLUENT 19.3 Theory Guide.

Assi, G.R., Bearman, P.W., Meneghini, J.R., 2010. On the wake-induced vibration of tandem circular cylinders: the vortex interaction excitation mechanism. J. Fluid Mech. 661, 365–401.
Assi, G.R., 2014. Wake-induced vibration of tandem and staggered cylinders with two degrees of freedom. J. Fluid Struct. 50, 340–357.
Carmo, B.S., Sherwin, S.J., Bearman, P.W., Willden, R.H.J., 2011. Flow-induced vibration of a circular cylinder subjected to wake interference at low Reynolds number. J. Fluid Struct. 27 (4), 503–522.
Dao, T., Yagi, T., Noguchi, K., Fukushima, H., Mohallem, G., Do, T., 2022. Generation mechanism of wake galloping in two staggered circular cylinders in view of hysteretic flow phenomena. J. Wind Eng. Ind. Aerod. 229, 105127.
Du, X., Dai, C., Wang, G., Chen, S., 2018. Experimental study on wake-induced vibrations of two circular cylinders with two degrees of freedom. Wind Struct. 26 (2), 57–68.
Fehér, R., Avila, J.P.J., 2022. Parametric behavior of a vortex-induced vibration model of cylinders with two degrees-of-freedom using a wake oscillator. J. Offshore Mech. Arctic Eng. 144, 021905.
Fukushima, H., Yagi, T., Shimoda, T., Noguchi, K., 2021. Wake-induced instabilities of parallel circular cylinders with tandem and staggered arrangements. J. Wind Eng. Ind. Aerod. 215, 104697.
Griffith, M.D., Jacono, D.L., Sheridan, J., Leontini, J.S., 2017. Flow-induced vibration of two cylinders in tandem and staggered arrangements. J. Fluid Mech. 833, 98–130.
Ishihara, T., Li, T., 2020. Numerical study on suppression of vortex-induced vibration of circular cylinder by helical wires. J. Wind Eng. Ind. Aerod. 197, 104081.
Jauvtis, N.A., Williamson, C.H.K., 2004. The effect of two degrees of freedom on vortex-induced vibration at low mass and damping. J. Fluid Mech. 509, 23–62.
Kang, Z., Zhang, C., Ma, G., Ni, W., 2018. A numerical investigation of two-degree-of-freedom VIV of a circular cylinder using the modified turbulence model. Ocean Eng. 155, 211–226.
Li, S., Xiao, C., Wu, T., Chen, Z., 2019. Aerodynamic interference between the cables of the suspension bridge hanger. Adv. Struct. Eng. 22 (7), 1657–1671.
Li, T., Yang, Q., Ishihara, T., 2018. Unsteady aerodynamic characteristics of long-span roofs under forced excitation. J. Wind Eng. Ind. Aerod. 181, 46–60.
Li, T., Ishihara, T., 2021a. Numerical study on wake galloping of tandem circular cylinders considering the effects of mass and spacing ratios. J. Wind Eng. Ind. Aerod. 210, 104536.
Li, T., Ishihara, T., 2021b. Numerical study on vortex-induced vibration of circular cylinder with two-degree-of-freedom and geometrical nonlinear system. J. Fluid Struct. 107, 103415.
Martins, F.A.C., Avila, J.P.J., 2019. Effects of the Reynolds number and structural damping on vortex-induced vibrations of elastically-mounted rigid cylinder. Int. J. Mech. Sci. 156, 235–249.
Menter, F.R., 1994. Two-equation eddy-viscosity turbulence models for engineering applications. AIAA J. 32 (8), 1598–1605.
Mittal, S., Kumar, V., 2001. Flow-induced oscillations of two cylinders in tandem and staggered arrangements. J. Fluid Struct. 15 (5), 717–736.
Mysa, R.C., Kaboudian, A., Jaiman, R.K., 2016. On the origin of wake-induced vibration in two tandem circular cylinders at low Reynolds number. J. Fluid Struct. 61, 76–98.
Nguyen, V.T., Chan, W.H.R., Nguyen, H.H., 2018. Numerical investigation of wake induced vibrations of cylinders in tandem arrangement at subcritical Reynolds numbers. Ocean Eng. 154, 341–356.
Oka, S., Ishihara, T., 2020. A study of galloping analysis of ice-accreted transmission line considering unsteady aerodynamic forces. J. Wind Eng. JAWE 45 (2), 27–41 (In Japanese).
Price, S.J., Piperni, P., 1988. An investigation of the effect of mechanical damping to alleviate wake-induced flutter of overhead power conductors. J. Fluid Struct. 2 (1), 53–71.
Qin, B., Alam, M.M., Zhou, Y., 2019. Free vibrations of two tandem elastically mounted cylinders in crossflow. J. Fluid Mech. 861, 349–381.
Sarpkaya, T., 2004. A critical review of the intrinsic nature of vortex-induced vibrations. J. Fluid Struct. 19 (4), 389–447.
Xu, W., Wu, H., Jia, K., Wang, E., 2021. Numerical investigation into the effect of spacing on the flow-induced vibrations of two tandem circular cylinders at subcritical Reynolds numbers. Ocean Eng. 236, 109521.
Yagi, T., Arima, M., Araki, S., Ogawa, S., Kosugi, T., Zain, M.R.M., Shirato, H., 2015. Investigation on wake-induced instabilities of parallel circular cylinders based on unsteady aerodynamic forces. In: Proc. Of 14th International Conference on Wind Engineering, pp. 1–12. Porto Alegre, Brazil.
Yu, K.R., Étienne, S., Scolan, Y.M., Hay, A., Fontaine, E., Pelletier, D., 2016. Flow-induced vibrations of in-line cylinder arrangements at low Reynolds numbers. J. Fluid Struct. 60, 37–61.